

Article

Exploration of ZnO-Doped Nitrogen-Carbon Materials Derived from Polyamide-Imide for Propane Dehydrogenation

Huahua Zhao ¹, Tingyu Ji ², Yanping Wu ³, Huanling Song ¹, Jianfeng Wu ^{1,2,*} and Lingjun Chou ^{1,*}

¹ State Key Laboratory for Oxo Synthesis and Selective Oxidation, Lanzhou Institute of Chemical Physics, Chinese Academy of Sciences, Lanzhou 730000, China; hhzhao@licp.cas.cn (H.Z.); songhl@licp.cas.cn (H.S.)

² State Key Laboratory of Applied Organic Chemistry, Key Laboratory of Nonferrous Metals Chemistry and Resources Utilization of Gansu Province, College of Chemistry and Chemical Engineering, Lanzhou University, Lanzhou 730000, China; jity17@lzu.edu.cn

³ Key Laboratory of Science and Technology on Wear and Protection of Materials, Lanzhou Institute of Chemical Physics, Chinese Academy of Sciences, Lanzhou 730000, China; wuy1012@licp.cas.cn

* Correspondence: wjfw@licp.cas.cn (J.W.); ljchou@licp.cas.cn (L.C.)

Abstract: A series of ZnO-doped nitrogen-carbon materials (xZnO-N-C) with ZnO contents of 5–40% are prepared by a vacuum curing–carbonization strategy using polyamide-imide as the N-C source and zinc nitrate as the metal source for propane dehydrogenation (PDH). 20ZnO-N-C exhibits outstanding initial activity (propane conversion of 35.2% and propene yield of 24.6%) and a relatively low deactivation rate (0.071 h^{−1}) at 600 °C. The results of detailed characterization show that small ZnO nanoparticles (5.5 nm) with high dispersion on the catalyst can be obtained by adjusting the ZnO loading. Moreover, more nitrogen-based species, especially ZnN_x species, are formed on 20ZnO-N-C in comparison with 20ZnO-N-C-air prepared via curing carbonization without vacuum, which may contribute to the higher product selectivity and catalytic stability of 20ZnO-N-C. The active sites for the PDH reaction on the catalyst system are proposed to be C=O species and Zn²⁺ species. Moreover, the carbon deposition and the aggregation of ZnO nanoparticles are the causes of activity loss on this catalyst system.

Keywords: polyamide-imide; ZnO-doped nitrogen-carbon; propane dehydrogenation; propene



Citation: Zhao, H.; Ji, T.; Wu, Y.; Song, H.; Wu, J.; Chou, L. Exploration of ZnO-Doped Nitrogen-Carbon Materials Derived from Polyamide-Imide for Propane Dehydrogenation. *Inorganics* **2024**, *12*, 22. <https://doi.org/10.3390/inorganics12010022>

Academic Editor: Paolo Fornasiero

Received: 27 November 2023

Revised: 14 December 2023

Accepted: 21 December 2023

Published: 2 January 2024



Copyright: © 2024 by the authors. Licensee MDPI, Basel, Switzerland. This article is an open access article distributed under the terms and conditions of the Creative Commons Attribution (CC BY) license (<https://creativecommons.org/licenses/by/4.0/>).

1. Introduction

The selective activation of the inert but ubiquitous C–H bond in hydrocarbon molecules remains of utmost importance, posing a formidable challenge in catalysis and even in the field of chemistry [1,2]. Light alkenes, such as propylene, as key raw materials and primary products of the petrochemical industry, have attracted ever-increasing attention [3]. Propylene is one of the basic feedstocks for the production of plastics, packaging materials, and synthetic fibers in the global chemical industry. Therefore, propylene production technology, especially propane dehydrogenation (PDH), is of great interest to the petrochemical market to expand the sources of propylene via a non-petroleum cracking route [4].

Owing to the highly endothermic characteristic of the PDH reaction, side reactions, including propane cracking, deactivation by coke formation, and metal sintering, easily occur under the required high temperature (550–600 °C), severely impeding its practical application [5]. Currently, the PDH reaction is heavily dependent in industry on the utilization of precious metals such as platinum and toxic transition metal oxides such as chromium oxide [6]. Therefore, it is highly attractive to explore a low-cost and nontoxic catalyst material for PDH with industrial-level propylene selectivity and catalytic stability.

Many alternative catalyst systems including metal oxides such as VO_x, FeO_x, ZnO, metal sulfides, and carbon materials have been extensively developed, and their design concepts could provide important references for the development of an efficient dehydrogenation catalyst [7–12]. Recently, Zn species have been explored as active components

of dehydrogenation catalysts, in addition to their role as promoters [13–16]. Moreover, ZnO-based materials, such as ZnO loaded on silicalite-1 or doped with NbO, are usually synthesized via impregnation, ion-exchange, and the pulsed laser deposition method, which could exhibit good propane dehydrogenation performance [17–19]. In particular, it has been demonstrated that isolated Zn atoms or highly dispersed ZnO nanoclusters present high propene selectivity and catalytic stability in the PDH system [20]. Schweitzer et al. observed high propene selectivity for single-site Zn²⁺ on SiO₂, and pointed out that three-coordinated Zn²⁺ Lewis acid sites and the coordinated environment of metal oxides are of great significance in the design of efficient metal oxide catalysts for PDH [21]. Shi et al. found that ZnO nanoparticles with an appropriate size of approximately 4.8 nm on ZnO/SiO₂ exhibited the maximum PDH activity, and proposed that unsaturated Zn²⁺ accompanied by oxygen vacancies are the active sites for the activation of the C–H bond in propane [16]. However, ZnO-based materials have inherent stability defects due to the production of low-melting-point metallic Zn (420 °C) in the PDH reaction process. Also, some acidic supports such as molecular sieves may lead to the low propene selectivity and poor stability of Zn-based catalysts due to side reactions and coking [22]. To overcome these shortcomings, constructing strong coordination interactions between active Zn species and a support showing basicity, such as N-doped carbon material (N-C), is a feasible strategy. Notable examples of this are the design of highly dispersed Zn-based catalysts supported on N-C material from zeolitic imidazolate framework-8 [23,24]. Owing to the stabilizing effect of the N-C material on ZnO nanoparticles, the catalysts show high activity and stability for the PDH reaction. However, the nature of the catalytically active Zn sites in Zn-based N-C material is still poorly understood.

Polyamide-imide (PAI), as an important, well-established, and commercialized class of polymers, prepared via the condensation of an aromatic diamine and an anhydride, can be a good source for the synthesis of N-C material, which has a strong anchoring effect for metal species and favorable surface modifications [25,26]. However, little is known about the utilization of PAI as the precursor to prepare Zn-based N-C material for the PDH reaction. In this study, we developed a facile vacuum curing–carbonization approach to prepare a series of ZnO-doped N-C materials (ZnO-N-C) with small ZnO nanoparticles using PAI as the N-C source and zinc nitrate as the metal source. The relationship between the structure of the catalyst and the activity of the Zn species in the PDH reaction was explored using a series of characterization techniques. Moreover, the probable active sites and deactivation factors for the PDH reaction on the catalysts were determined and proposed.

2. Results and Discussion

2.1. The Phase Structure and Nanoparticle Size of the Catalyst

The phase structure of each catalyst was firstly characterized via XRD analysis, as shown in Figure 1. The sharp and strong peaks in the pattern of the ZnO catalyst, located at 2θ positions of 31.8°, 34.4°, 36.2°, 47.5°, 56.6°, 62.9°, 66.4°, 68.0°, 69.1°, 72.6°, and 77.0°, corresponded to the characteristic planes (100), (002), (101), (102), (110), (103), (200), (112), (201), (004), and (202) of the ZnO hexagonal phase, respectively (JCPDS No. 36-1451) [27]. Meanwhile, the broad diffraction peak at 22.4°, corresponding to the (002) peak of graphite, was observed in the pattern of the N-C-based materials, demonstrating the amorphous carbon skeleton of the support [28]. Moreover, there was another weak and broad peak at 44.1°, attributed to the (100) reflection plane of graphitized carbon [29,30]. This means that the N-C-based catalysts were in a certain degree of graphitization, consistent with the following Raman results. There were no signals about the ZnO phase for 5ZnO-N-C, indicating its high dispersion on the catalyst. When further increasing the loading amount of ZnO to 10%, in sharp contrast, the featured high-intensity diffraction peaks of ZnO appeared, indicating the successful synthesis of ZnO-doped nitrogen-carbon material derived from PAI. After careful calculation using the Debye–Scherer equation, the grain size of ZnO for 10ZnO-N-C was found to be 29.5 nm. However, further increasing the ZnO content to 20–40%, the diffraction peaks attributed to ZnO became weak and broad,

suggesting the higher dispersion of ZnO nanoparticles on the catalysts. The grain sizes of ZnO were 5.1–7.4 nm on the 20–40ZnO-N-C catalysts, much smaller than those on 10ZnO-N-C. Notably, there was an exceptional case in which the characteristic peaks belonging to ZnO in the XRD pattern of 10ZnO-N-C were obviously sharper than those of the other catalysts with a higher ZnO content. It was carefully observed that considerably more foam was generated during the curing process of 10ZnO-N-C compared with during the curing process of other catalysts with different ZnO contents, which indicated that the violent reaction easily caused zinc enrichment on the catalyst surface, resulting in the agglomeration of ZnO species, which was further observed in the following TEM images. By comparison, the pure ZnO catalyst exhibited a very large ZnO grain size of 62.4 nm, suggesting that loading ZnO onto the N-C material could severely reduce its grain size, thus improving its dispersion. Moreover, after carefully comparing the XRD diffraction peaks of 20ZnO-N-C and 20ZnO-N-C-air, as expected, the grain size of ZnO on 20ZnO-N-C-air (12.9 nm) was found to be more than twice larger than that on 20ZnO-N-C (5.1 nm), suggesting the higher dispersion of ZnO nanoparticles on the latter.

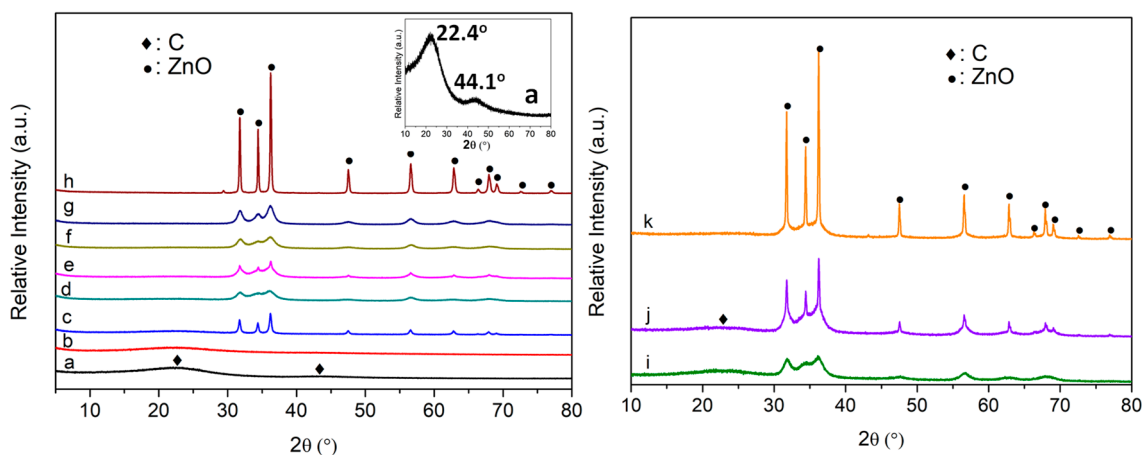


Figure 1. XRD patterns of the fresh catalysts: (a) N-C; (b) 5ZnO-N-C; (c) 10ZnO-N-C; (d) 20ZnO-N-C; (e) 20ZnO-N-C-air; (f) 30ZnO-N-C; (g) 40ZnO-N-C; (h) ZnO. XRD patterns of the spent catalysts: (i) 20ZnO-N-C (GHSV = 840 h⁻¹, T = 600 °C, t = 2.5 h); (j) 20ZnO-N-C (GHSV = 840 h⁻¹, T = 580 °C, t = 6 h); (k) 20ZnO-N-C-air (GHSV = 840 h⁻¹, T = 600 °C, t = 2.5 h).

To determine the nanoparticle size and state of the ZnO on the catalysts, TEM and HRTEM images are depicted in Figure 2. A large bulk structure with a smooth surface was observed on the N-C catalyst/support. As expected, no ZnO nanoparticles could be observed for the 5ZnO-N-C catalyst because of its high dispersion on the catalyst, consistent with the XRD result. However, there were many accumulated ZnO nanoparticles with extremely heterogeneous distribution on the carbon support for 10ZnO-N-C. From the statistics, the average size of ZnO nanoparticles was 35.9 nm. Further increasing the ZnO content to 20–40%, it was observed that the ZnO nanoparticles were highly dispersed on the catalysts. And, the nanoparticle size was 5.5 nm, 6.8 nm, and 8.2 nm for 20ZnO-N-C, 30ZnO-N-C, and 40ZnO-N-C, respectively. In comparison with 20ZnO-N-C, 20ZnO-N-C-air exhibited a larger ZnO nanoparticle size of 13.8 nm, demonstrating the higher dispersion of ZnO nanoparticles on 20ZnO-N-C. However, the series of the above-mentioned catalysts showed a much smaller nanoparticle size than the pure ZnO catalyst (221.0 nm), suggesting that loading ZnO onto the N-C support significantly hindered the growth of the ZnO nanoparticles, also having a stabilization effect on the N-C material [23]. Moreover, the HRTEM observations of the catalysts showed that there were two exposed crystalline planes with an interplanar spacing of 0.284 nm and 0.264 nm, belonging to the characteristic ZnO (100) and ZnO (002) planes, respectively [31,32].

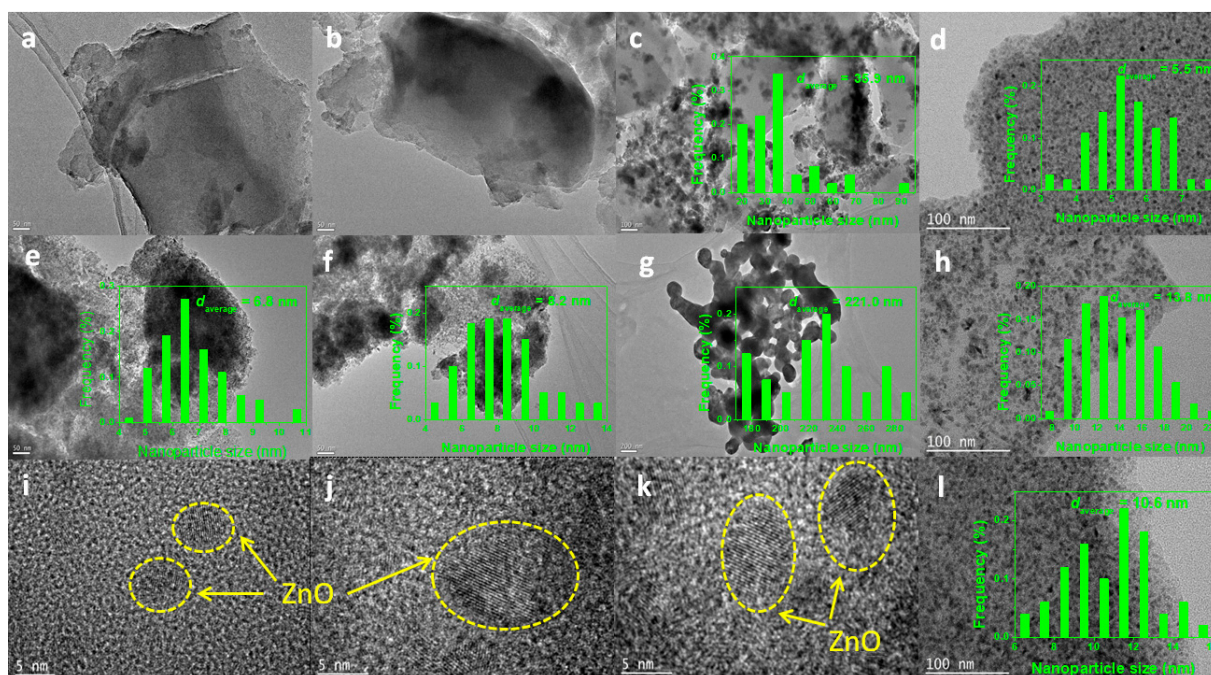


Figure 2. TEM images of (a) N-C; (b) 5ZnO-N-C; (c) 10ZnO-N-C; (d) 20ZnO-N-C; (e) 30ZnO-N-C; (f) 40ZnO-N-C; (g) ZnO; (h) 20ZnO-N-C-air; (i) spent 20ZnO-N-C catalyst (GHSV = 840 h⁻¹, T = 580 °C, t = 6 h). HRTEM images of (i) 20ZnO-N-C; (j) 20ZnO-N-C-air; (k) spent 20ZnO-N-C catalyst (GHSV = 840 h⁻¹, T = 580 °C, t = 6 h).

The Raman spectra of the catalysts were further analyzed and are described in Figure 3. No characteristic Raman bands of ZnO between 200 cm⁻¹ and 600 cm⁻¹ were observed on the catalysts, also suggesting that the ZnO nanoparticles were doped on the support [33]. However, all the catalysts exhibited the featured D band and G band at 1345 cm⁻¹ and 1590 cm⁻¹, which are attributed to the structural defect of the carbon atomic lattice and the in-plane stretching vibration of carbon atom sp² hybridization [34,35]. The I_D/I_G values for Raman spectra were utilized to evaluate the graphitization of carbon-based materials, which are listed in Figure 3. In comparison with N-C, the introduction of ZnO caused the I_D/I_G value to slightly increase from 1.48 to 1.61–1.70, suggesting that ZnO destroyed the order of the carbon materials, thus resulting in the reduction in the graphitization degree of the carbon-based catalysts. With the further increase in ZnO content in the catalyst, the I_D/I_G value changed little, indicating that adjusting the ZnO content did not have a significant effect on the graphitization of the carbon materials.

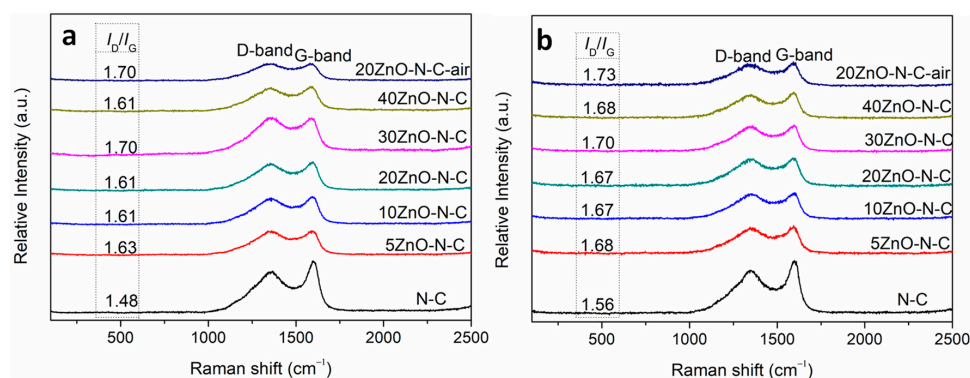


Figure 3. Raman spectra of (a) fresh and (b) spent catalysts (GHSV = 840 h⁻¹, T = 580 °C, t = 6 h).

2.2. The Surface Composition and State of the Catalyst

FTIR spectra were recorded to identify the types of functional groups on the catalysts, which are depicted in Figure 4. The figure shows that all catalysts with different ZnO contents display similarly shaped curves. The vibration of O–H located at the wavenumber of 3432 cm^{-1} was observed [36], indicating the presence of adsorbed H_2O molecules on the catalyst surface, consistent with the following XPS results. The stretching vibrations located at about $2810\text{--}3010\text{ cm}^{-1}$ correspond to the C–H bond [34]. The peaks at 1580 cm^{-1} and 1280 cm^{-1} can be attributed to C=N bond and N–H bond [37], indicating that N-containing species were successfully retained in the catalyst. The intensive bands around 1726 cm^{-1} belong to the stretching vibrations of the C=O group, which is usually recognized as the active site of PDH on carbon-based materials [38,39]. However, the intensity of the C=O bond in the spectra of 20ZnO-N-C was the weakest among all the catalysts, indicating that C=O species may not have been the sole active site in the catalyst system for the PDH reaction.

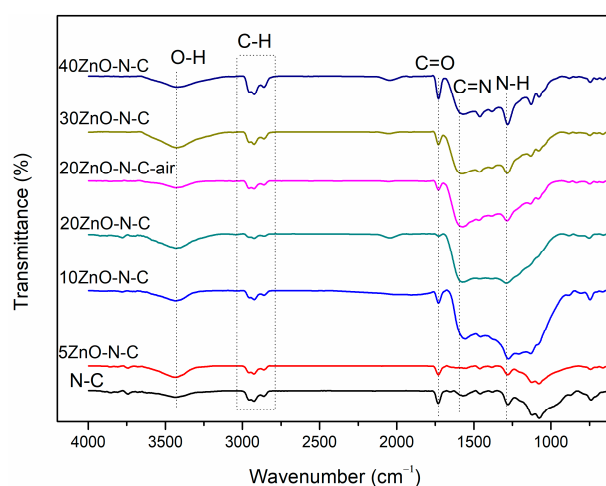


Figure 4. FTIR spectra of the fresh catalysts.

Furthermore, the XPS spectra of the catalysts, shown in Figure 5, were obtained to detect the elemental composition and chemical state of the species on the catalyst surface. The spectra revealed the presence of Zn, N, O, and C on $x\text{ZnO-N-C}$ catalyst's surface, demonstrating that Zn species were successfully loaded, and N species were maintained in the materials. The two peaks located at $1021.6\text{--}1022.3\text{ eV}$ and $1044.8\text{--}1045.5\text{ eV}$ were assigned to the $2p_{3/2}$ and $2p_{1/2}$ electronic states of Zn^{2+} , respectively [27]. The binding energy of Zn 2p for ZnO obviously shifted to higher direction in the $x\text{ZnO-N-C}$ and 20ZnO-N-C-air catalysts, indicating that the interactions between Zn species and the N-C support such as through Zn– N_x coordination bonds formed during the preparation process. Moreover, the intensity of the Zn 2p spectra strengthened for the $x\text{ZnO-N-C}$ catalyst with increasing ZnO content, demonstrating that the Zn content on the catalyst surface increased, as listed in Table 1. The N 1s spectra of the N-C was clearly split into three peaks at 398.6 eV , 400.6 eV , and 401.5 eV , which are associated with pyridinic-N, pyrrolic-N, and graphitic-N species, respectively [40]. However, the deconvoluted N 1s spectra of the $x\text{ZnO-N-C}$ and 20ZnO-N-C-air revealed that another type of nitrogen-based species Zn– N_x , located at 399.4 eV , was present [15]. Therefore, the results confirmed that Zn– N_x species formed in the carbon skeleton of $x\text{ZnO-N-C}$. Moreover, 20ZnO-N-C exhibited a larger total amount of the three nitrogen-based species (5.71%) and surface Zn– N_x species (1.14%) than 20ZnO-N-C-air, which may have resulted from the more thorough condensation reaction that occurred under a vacuum compared with that in air. The O 1s signals of the catalysts exhibited three distinct peaks: lattice O (O_{lat} : $530.4\text{--}530.7\text{ eV}$) or Zn–O from ZnO, O defect (O_{def} : $532.0\text{--}532.3\text{ eV}$), or the O species of C=O group on the N-C support and adsorbing O (O_{ad} : $533.4\text{--}533.7\text{ eV}$), or adsorbed H_2O molecules [41]. As shown in Table 1, the content of surface O species on 20ZnO-N-C was less than on 20ZnO-N-C-air, which we attributed to

the C=O groups, suggesting that the C=O group was not the only active site for the PDH reaction, consistent with the FTIR results.

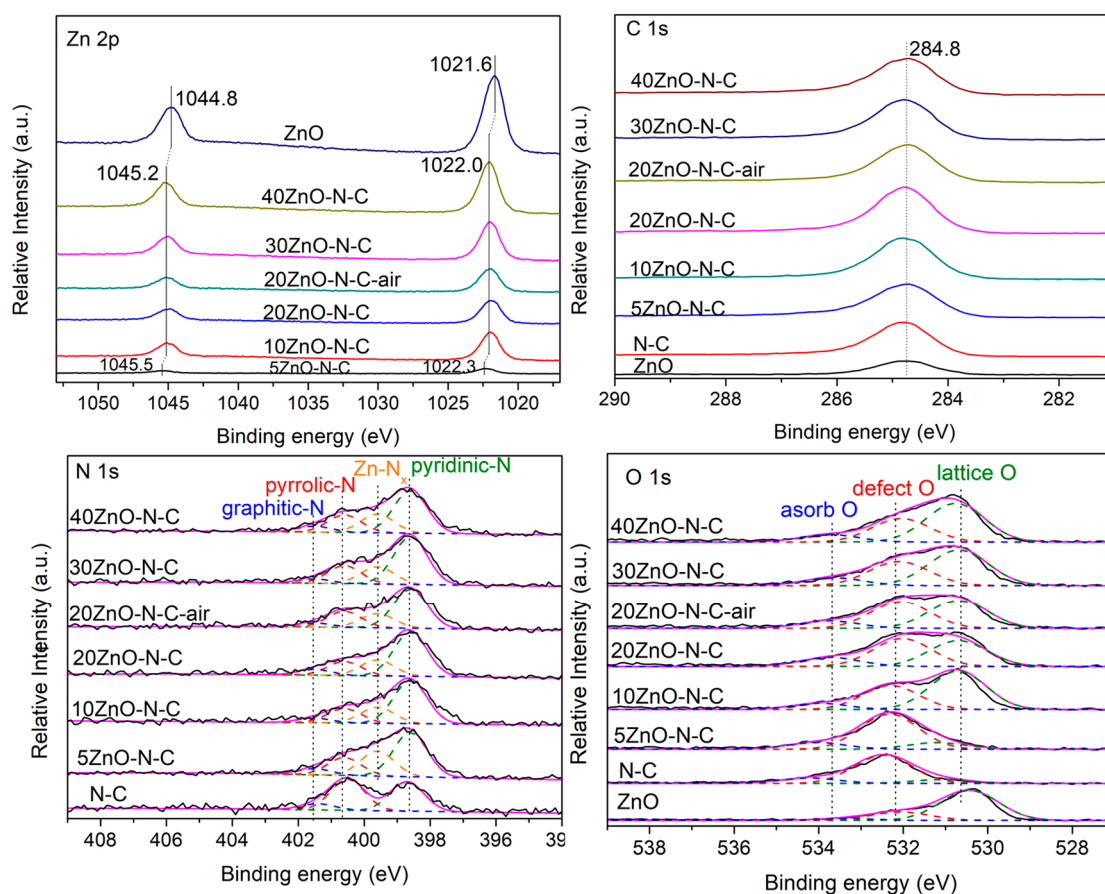


Figure 5. XPS spectra of the fresh catalysts.

Table 1. The contents of surface species on the fresh catalysts based on the XPS results.

Catalyst	Atomic Content (%)								
	Zn	N				O	C		
		Pyridinic-N	Zn-N _x	Pyrrrole-N	Graphitic-N	Zn-O	C=O	O-H	
N-C	0	1.62	0	1.72	0.34	0	6.96	2.02	87.36
5ZnO-N-C	1.46	3.44	1.95	1.39	0.48	1.29	6.02	1.25	82.73
10ZnO-N-C	6.52	2.77	1.04	0.93	0.29	5.37	3.78	1.09	78.20
20ZnO-N-C	5.26	3.16	1.14	1.02	0.40	4.32	4.20	1.02	79.49
30ZnO-N-C	8.48	3.30	1.19	1.25	0.30	6.63	4.86	1.22	72.76
40ZnO-N-C	10.73	3.04	1.34	1.26	0.43	8.20	4.66	1.33	69.02
20ZnO-N-C-air	6.27	2.45	0.88	0.99	0.25	5.53	5.39	1.58	76.68

2.3. The Acidity and Basicity of the Catalysts

The acidity and basicity of a catalyst are important factors influencing its dehydrogenation activity and product selectivity [42]. Therefore, NH₃-TPD and CO₂-TPD characterizations were performed for each catalyst in order to detect their acidity and basicity, and the corresponding profiles are displayed in Figure 6. The peaks with weak intensities, located at 100–350 °C on the NH₃-TPD and CO₂-TPD profiles of the xZnO-N-C and 20ZnO-N-C-air catalysts, suggested the presence of tiny amounts of acidity and basicity [43]. Both ZnO and N-C materials are hardly acidic or basic. After ZnO loading, the materials exhibited increasing acidity and basicity, demonstrating that there were some interactions between

Zn and N-C species, as proved by the Raman and XPS characterizations. Moreover, the acidity and basicity of xZnO-N-C varied for different ZnO loading amounts, suggesting that Zn loading can be utilized to adjust the acidic and basic sites of N-C-based materials.

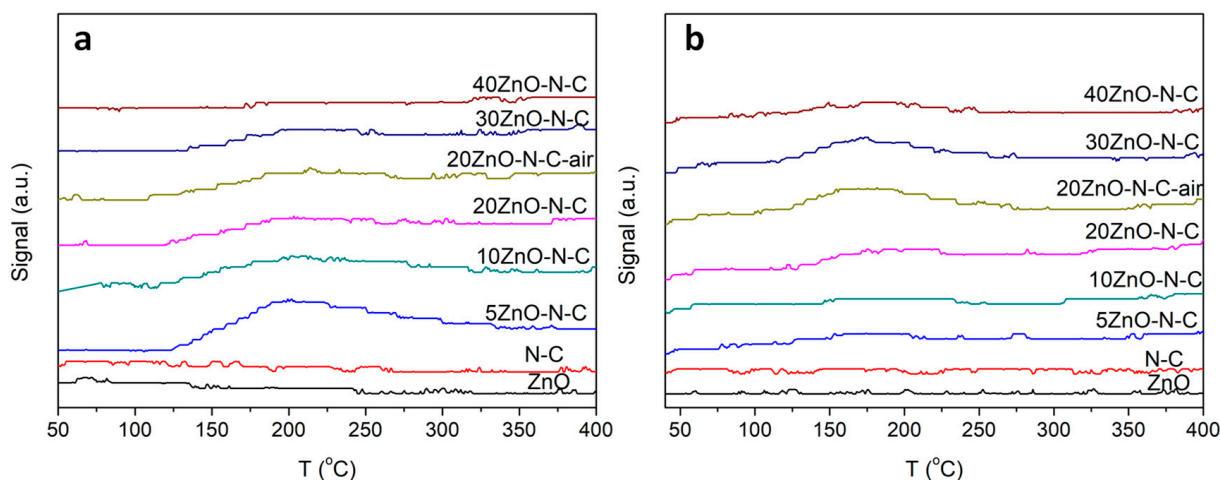


Figure 6. (a) NH₃-TPD and (b) CO₂-TPD profiles of the fresh catalysts.

2.4. Catalytic Performance and Stability for PDH

The catalytic performance of the above-mentioned materials in the PDH reaction was firstly investigated, and the results are illustrated in Figure 7 and Table 2. Both ZnO and N-C catalysts produced a propane conversion of about 20.0%, indicating that ZnO species and C=O species both provided active sites for the PDH reaction [20,44]. By comparison, the N-C material exhibited slightly higher propene selectivity (46.5%) than the ZnO catalyst. For the 20ZnO-N-C-air catalyst, the propane conversion and propylene selectivity both increased 32.1% and 53.4%, which may be due to the coevaluation of acidity and basicity of the catalyst, caused by the formation of Zn–N_x coordination bonds and the presence of electron-donating function groups such as nitrogen-based species. In sharp contrast, however, the 20ZnO-N-C catalyst presented advantages in terms of product selectivity and catalytic stability. Specifically, a higher propene selectivity (70.0%) with a propane conversion of 35.2% was obtained, suggesting that the larger number of electron-donating groups on 20ZnO-N-C led the electron-rich product of propene to easily desorb from the catalyst surface, thus improving the product selectivity. Regarding catalytic stability, 20ZnO-N-C had the smaller deactivation rate constant ($k_d = 0.10 \text{ h}^{-1}$) than 20ZnO-N-C-air ($k_d = 0.38 \text{ h}^{-1}$), demonstrating the higher stability of the former. And, the formation of strong Zn–N_x coordination bonds was conducive to the improvement in the catalytic stability. Moreover, the propene selectivity gradually increased; thus, the propene yield reached the maximum (27.3%) after 60 min of reaction, then gradually decreased to 24.0% on the 20ZnO-N-C catalyst during the 150 min reaction. This trend was similar to that of the initial propene yield (24.6%), also indicating the higher catalytic stability of the catalyst. By comparison, the propene yield of 20ZnO-N-C-air continuously decreased from 17.1% to 10.0% during the 150 min reaction. With the increase in ZnO loading, both the propane conversion and propene selectivity first increased and then decreased, demonstrating that the ZnO content of the catalyst affected the catalytic performance for PDH.

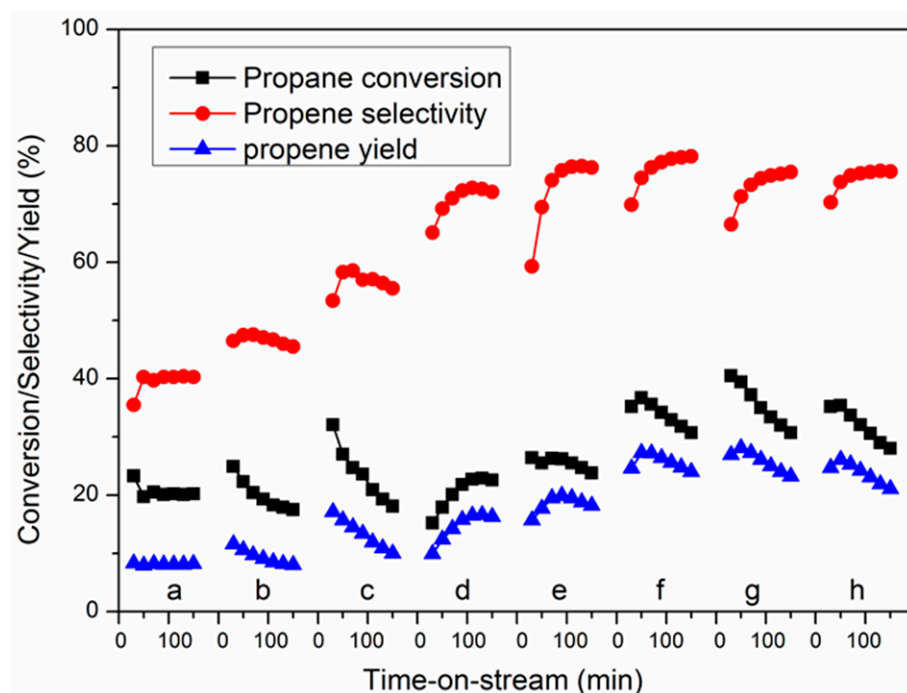


Figure 7. The catalytic performance of (a) ZnO; (b) N-C; (c) 20ZnO-N-C-air; (d) 5ZnO-N-C; (e) 10ZnO-N-C; (f) 20ZnO-N-C; (g) 30ZnO-N-C; (h) 40ZnO-N-C. Reaction conditions: GHSV = 840 h⁻¹, T = 600 °C.

Table 2. The results obtained from propane dehydrogenation over Zn-based catalysts.

Catalyst	Gas Composition	GHSV _{C₃H₈} (h ⁻¹)	T (°C)	C ₃ H ₈ Conversion (%)	C ₃ H ₆ Selectivity (%)	k _d (h ⁻¹)	Reference
Zn/H-ZSM-5(15, 1.3)	C ₃ H ₈ /N ₂ = 5/95	20,000	550	~13	~80	-	[20]
5ZnO/SiO ₂	H ₂ /C ₃ H ₈ /Ar = 1/1/5	1000	600	27	95	0.030	[16]
ZnO@NC/S-1(1.0)	H ₂ /C ₃ H ₈ /N ₂ = 1/1/5	450	600	44.4	90	0.092	[23]
NS-ZIF8-900	C ₃ H ₈ /He = 1/4	1860	550	~5	~88	-	[24]
		930	600	~15	~80	0.082	
20ZnO-N-C	C ₃ H ₈ (100%)	840	580	18.1	83	0.071	This work
		840	600	30.7	78.2	-	This work

Note: C₃H₈ conversion and C₃H₆ selectivity are provided as stable values, with the time-on-stream reported.

Then, the influences of reaction temperature (T) and gas hourly space velocity (GHSV) of propane for the 20ZnO-N-C catalyst on the PDH reaction were determined, as shown in Figure 8. As expected, propane conversion greatly increased and the propene selectivity of the catalyst gradually reduced as the reaction temperature increased from 560 °C to 620 °C based on the endothermic characteristic of the PDH reaction. Moreover, the k_d value of 20ZnO-N-C increased, illustrating a decreasing catalytic stability with increasing reaction temperature. Also, as expected, the propane conversion of the catalyst gradually decreased, and the propene selectivity and catalytic stability increased as the GHSV of propane increased from 600 h⁻¹ to 1200 h⁻¹. This occurred because the reduction in the contact time prevented the occurrence of side reactions, therefore benefiting the propylene selectivity and thus the catalytic stability.

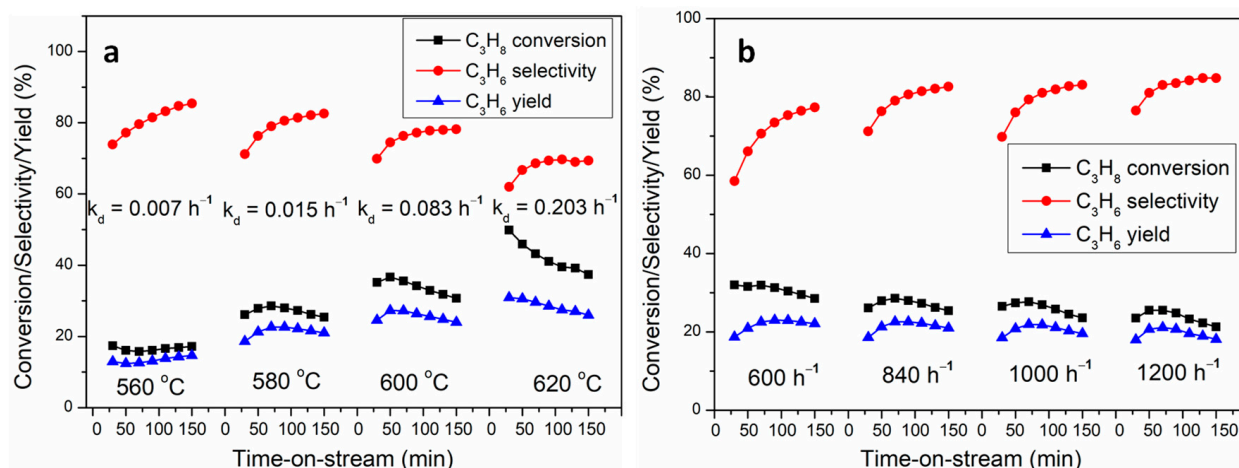


Figure 8. The catalytic performance of 20ZnO-N-C at (a) different temperatures with the same GHSV = 840 h⁻¹ and (b) different GHSVs at the same temperature $T = 580$ °C.

Finally, the catalytic stability of the 20ZnO-N-C catalyst at a reaction temperature of 580 °C and a GHSV of 840 h⁻¹ was determined over 6 h, with the results presented in Figure 9. The initial propane conversion and propene selectivity were 24.6% and 68.6% for the catalyst, respectively. With the increase in the time-on-stream, propane conversion shows a slightly decreased trend with a very small k_d value of 0.071 h⁻¹. Nevertheless, the propene selectivity ascended, reached 83.0% after reaction for about 150 min, and then stabilized, demonstrating the high stability of the 20ZnO-N-C catalyst under reaction conditions of $T = 580$ °C and GHSV = 840 h⁻¹.

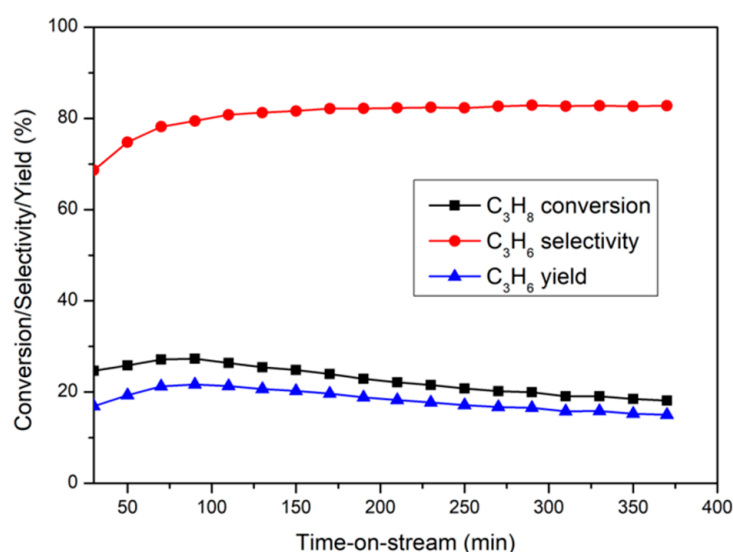


Figure 9. The catalytic performance of 20ZnO-N-C at GHSV = 840 h⁻¹, $T = 580$ °C.

2.5. The Deactivation of the Catalyst

The deactivation of the PDH catalyst can be caused by coke formation and the aggregation of active nanoparticles on the catalyst [4,45]. As a consequence, the Raman spectra of the spent catalysts after 150 min of reaction were collected and are shown in Figure 3. It can be observed that the I_D/I_G value slightly increased from 1.48–1.70 of the fresh catalyst to 1.56–1.73 of the spent catalyst, demonstrating coke formation on the spent catalysts. Moreover, the deposited carbon was mainly amorphous.

In order to investigate the amount of coke on the spent catalysts, the TG curves of the fresh and spent N-C, 20ZnO-N-C-air, and 20ZnO-N-C ($T = 600$ °C, GHSV = 840 h⁻¹,

$t = 150$ min) were recorded and are shown in Figure 10. The amount of coke was calculated using the weight loss between 300 °C and 700 °C. The amount of the deposited carbon for the N-C catalyst was 8.2 wt%. The 20ZnO-N-C-air catalyst deposited 10.3 wt% carbon. We found that the 20ZnO-N-C catalyst exhibited slightly more coke accumulation (12.6 wt%) than 20ZnO-N-C-air. In combination with the catalytic performance, the coke formation is one of the factors that resulted in the decrease in activity, but it was probably not the main factor for the ZnO-N-C catalyst during the reaction.

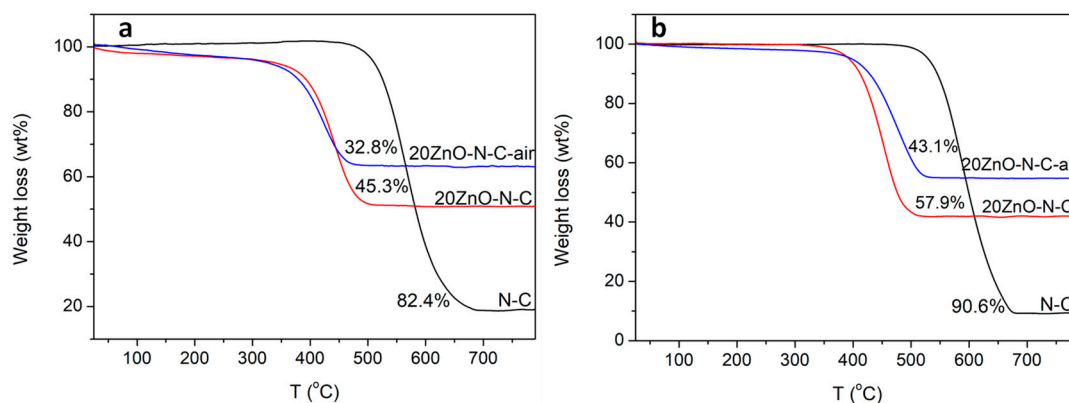


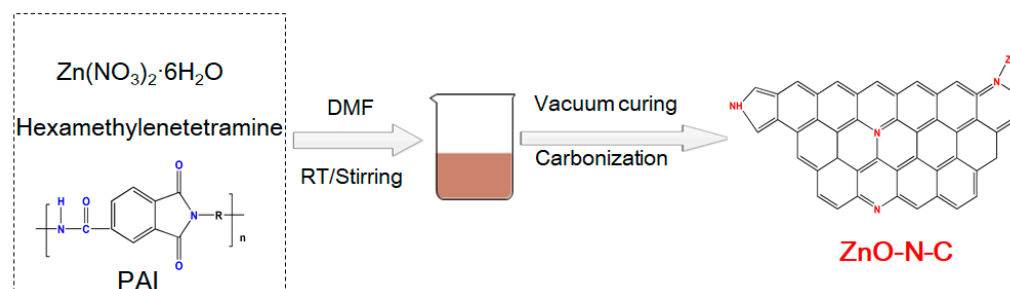
Figure 10. The TG curves of the (a) fresh and (b) spent catalysts at GHSV = 840 h⁻¹, $T = 600$ °C, $t = 2.5$ h.

In order to obtain information about the nanoparticle size of ZnO, the XRD patterns of some representative spent catalysts were recorded and are presented in Figure 1. The peak intensities belonging to the ZnO phase in the XRD pattern of the spent 20ZnO-N-C-air significantly strengthened compared with those of the fresh catalyst. And, the ZnO grain size grew from 12.9 nm to 57.6 nm during the reaction, demonstrating the serious sintering of ZnO after the reaction, which may have been another cause of the activity loss. For 20ZnO-N-C, the characteristic peak intensity of ZnO did not change significantly after the reaction, and the grain size of ZnO remain unchanged at about 5.0 nm. This finding clearly showed that the 20ZnO-N-C catalyst possessed better antisintering ability than the 20ZnO-N-C-air catalyst. Moreover, the nanoparticle size of ZnO grew from 5.5 nm on the fresh 20ZnO-N-C catalyst to 10.6 nm after 6 h of reaction, as shown in the TEM image (Figure 2), further demonstrating that nanoparticle aggregation was the primary reason for the activity loss on the catalyst system.

3. Experimental Procedure

3.1. Catalyst Preparation

A series of xZnO-N-C catalysts (where x is the weight percent of ZnO in the catalyst precursor) were prepared with a vacuum curing–carbonization process, as shown in Scheme 1. Taking 20ZnO-N-C as an example, the specific synthetic process was as follows: A mass of 4.00 g of PAI (SR3602-37W, US Cymer, solid content 38%, viscosity 5000 cps) was firstly dissolved in 30 mL of N,N-dimethylformamide (DMF, Sinopharm Chemical Reagent Co., Ltd., Shanghai, China) to form a transparent solution. Then, 3.66 g of Zn(NO₃)₂·6H₂O (Sinopharm Chemical Reagent Co., Ltd., Shanghai, China) and 1.00 g of hexamethylenetetramine (Sinopharm Chemical Reagent Co., Ltd., Shanghai, China) were added to obtain a homogeneous solution. This solution was then stirred at 150 °C to form a viscous solid and further cured under vacuum at 150 °C for 4 h to obtain the catalyst precursor. Finally, the precursor was carbonized at 500 °C for 2 h, then at 600 °C for 6 h in a N₂ atmosphere at a ramping rate of 1.5 °C·min⁻¹ to obtain the 20ZnO-N-C catalyst. The xZnO-N-C catalysts with ZnO weight percent of 5–40% were prepared following the process mentioned above by varying the added amount of PAI and Zn(NO₃)₂·6H₂O, respectively.

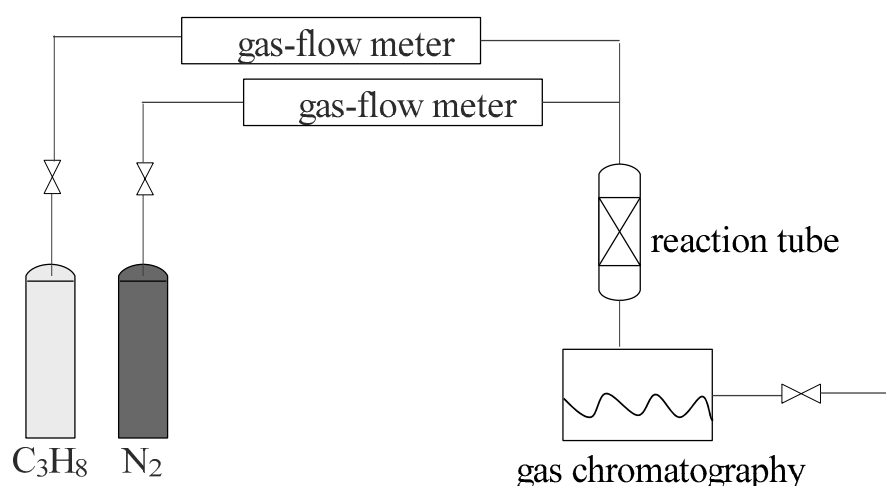


Scheme 1. The proposed ZnO-N-C catalyst formation mechanism.

As a comparison, 20ZnO-N-C-air was prepared via a similar process to that described above except that the obtained homogenous solution containing the same amount of PAI and $\text{Zn}(\text{NO}_3)_2 \cdot 6\text{H}_2\text{O}$ in DMF was cured at 240 °C for 3 h in atmospheric air in order to obtain the material with less nitrogen-based species. Moreover, N-C material with only adding PAI, and ZnO material without adding PAI, were also prepared by the same process mentioned above.

3.2. Catalytic Evaluation

The direct dehydrogenation of propane to propene was carried out in a continuous-flow quartz reaction tube at atmospheric pressure, packed with 0.50 g of catalyst sample supported on 1.0 g of quartz sand (60–80 mesh) and placed in the constant-temperature zone of a reaction furnace, as depicted in Scheme 2. Propane gas (5.0–10.0 mL·min⁻¹ flowing rate for 600–1200 h⁻¹ of GHSV) was switched into the reactor after the reaction temperature reached the set value in N₂ flow (20 mL·min⁻¹). The outlet gas was analyzed using an online gas chromatography (GC2014, SHIMADZU, Tokyo, Japan) equipped with a hydrogen flame ionization detector packed with HP-AL/S capillary chromatographic column and a thermal conductivity detector provided with TDX-01 packed column, with a sampling interval of 20 min. The carbon balance for all reactions was stabilized within the range of 100 ± 4%. Moreover, the deactivation rate constant (k_d , h⁻¹) of the catalyst was calculated using the following formula: $k_d = (\ln((1 - X_{\text{final}})/X_{\text{final}}) - \ln((1 - X_{\text{initial}})/X_{\text{initial}}))/t$, where X_{initial} and X_{final} represent the conversion of propane on the catalyst before and after reaction (%), and t stands for the reaction time (h).



Scheme 2. The general view of the dehydrogenation of propane to propene.

3.3. Catalyst Characterizations

The X-ray diffraction (XRD) of the samples was recorded with an X' Pert Pro multipurpose diffractometer (Smartlab-SE, Rigaku Corporation, Tokyo, Japan) with Cu-K α radiation ($\lambda = 0.15418$ nm) from 5° to 80° at room temperature.

Raman spectra of the catalysts were collected on a LabRam HR Evolution (HORIBA Jobin Yvon S.A.S., Paris, France) equipped with a CCD detector and laser excitation ($\lambda = 532$ nm) from 100 cm^{-1} to 2500 cm^{-1} .

Transmission electron microscopy (TEM) and high-resolution transmission electron microscopy (HRTEM) of the catalysts were performed with a transmission electron microscope (TECNAI G² F20, FEI, Hillsboro, OR, USA) at 200 kV.

Fourier transform infrared spectroscopy (FTIR) of the catalysts was operated at wavenumbers from 4000 to 500 cm^{-1} on a Nicolet Nexus 870 instrument (Nicolet Instruments, Madison, WI, USA).

X-ray photoelectron spectroscopy (XPS) analyses of the catalysts were performed on a Thermo Fisher Scientific K-Alpha spectrometer (Waltham, MA, US). The binding energy (BE) of the elements in the samples was determined referring to the C 1s peak (284.8 eV).

NH_3 and CO_2 temperature-programmed desorption of the catalysts (NH_3 -TPD and CO_2 -TPD) was undertaken on a ChemBET Pulsar TPR/TPD analyzer (Quantachrome, Boynton Beach, FL, USA). Before the test, 50 mg of catalyst was pretreated to remove the adsorbed impurity at $400\text{ }^\circ\text{C}$ for 60 min in He flow, followed by cooling to $100\text{ }^\circ\text{C}$ and switching to adsorb NH_3 or CO_2 for 60 min. After cooling to room temperature in He flow, NH_3 or CO_2 desorption was carried out under He gas at a ramping rate of $10\text{ }^\circ\text{C}\cdot\text{min}^{-1}$ to $900\text{ }^\circ\text{C}$.

Thermogravimetric (TG) measurements of the catalyst were determined on an NET-ZSCH STA 449F3 thermogravimetric analyzer (Selb, Germany) from room temperature to $800\text{ }^\circ\text{C}$ at a ramping rate of $10\text{ }^\circ\text{C}\cdot\text{min}^{-1}$ in air.

4. Conclusions

In conclusion, a facile vacuum curing–carbonization method involving the regulation of the Zn doping amount was developed for the production of $x\text{ZnO-N-C}$ materials with small ZnO nanoparticles, improving the C_3H_6 selectivity in propane dehydrogenation. Based on the structure–activity relationship, we found that Zn^{2+} species including Zn-N_x and C=O on the N-C support are the probable active sites for the PDH reaction. More nitrogen-based species, especially Zn-N_x coordination bonds, formed on $x\text{ZnO-N-C}$, leading to the coelevation of the activity and basicity of the materials. Consequently, the 20ZnO-N-C samples exhibited much higher initial activity (propane conversion of 35.2% and propene yield of 24.6%) and relatively lower deactivation rate (0.071 h^{-1}) than 20ZnO-N-C-air when prepared with the curing–carbonization process in a PDH reaction conducted at $600\text{ }^\circ\text{C}$. Furthermore, the catalyst deactivation was investigated, and carbon deposition and the aggregation of ZnO nanoparticles were found to be the causes of the activity loss in this catalyst system. The present findings provide not only a feasible construction strategy for the metal-oxide-doped nitrogen-carbon materials but also valuable guidance for the design of efficient catalysts for the dehydrogenation of light alkanes.

Author Contributions: H.Z. contributed to conceptualization, experimental design and performance, writing, and funding acquisition; T.J. contributed to data collection and formal analysis; Y.W. contributed to investigation and data curation; H.S. contributed to methodology and text editing. J.W. contributed to funding acquisition, conceptualization, and supervision; L.C. contributed to supervision and conceptualization. All authors have read and agreed to the published version of the manuscript.

Funding: This research was funded by the Lanzhou Institute of Chemical Physics (LICP) Cooperation Foundation for Young Scholars (HZJJ21-10), State Key Laboratory Program of Lanzhou Institute of Chemical Physics (LICP), Chinese Academy of Sciences (CHGZ-202209), National Natural Science Foundation of China (Nos. 21903041 and 21803027), and PetroChina Company Limited (LZSH-2022-JS-75).

Data Availability Statement: The data presented in this study are available on request from the corresponding author.

Conflicts of Interest: The authors declare that they have no known competing financial interests or personal relationships that could have appeared to influence the work reported in this paper. The funders of "PetroChina Company Limited (LZSH-2022-JS-75)" had no role in the design of the study;

in the collection, analyses, or interpretation of data; in the writing of the manuscript; or in the decision to publish the results.

References

1. van Koppen, P.A.M.; Bowers, M.T.; Haynes, C.L.; Armentrout, P.B. Reactions of ground-state Ti^+ and V^+ with propane: Factors that govern C-H and C-C bond cleavage product branching ratios. *J. Am. Chem. Soc.* **1998**, *120*, 5704–5712. [[CrossRef](#)]
2. Ali, W.; Prakash, G.; Maiti, D. Recent development in transition metal-catalysed C-H olefination. *Chem. Sci.* **2021**, *12*, 2735–2759. [[CrossRef](#)] [[PubMed](#)]
3. Waku, T.; Biscardi, J.A.; Iglesia, E. Active, selective, and stable Pt/Na-[Fe]ZSM5 catalyst for the dehydrogenation of light alkanes. *Chem. Commun.* **2003**, *14*, 1764–1765. [[CrossRef](#)]
4. Zhang, J.S.; Nakaya, Y.; Shimizu, K.; Furukawa, S. Surface engineering of titania boosts electroassisted propane dehydrogenation at low temperature. *Angew. Chem. Int. Ed.* **2023**, *62*, e202300744. [[CrossRef](#)] [[PubMed](#)]
5. Lu, J.L.; Fu, B.S.; Kung, M.C.; Xiao, G.M.; Elam, J.W.; Kung, H.H.; Stair, P.C. Coking- and sintering-resistant palladium catalysts achieved through atomic layer deposition. *Science* **2012**, *335*, 1205–1208. [[CrossRef](#)] [[PubMed](#)]
6. Sattler, J.J.H.B.; Ruiz-Martinez, J.; Santillan-Jimenez, E.; Weckhuysen, B.M. Catalytic dehydrogenation of light alkanes on metals and metal oxides. *Chem. Rev.* **2014**, *114*, 10613–10653. [[CrossRef](#)] [[PubMed](#)]
7. Sun, Y.N.; Wu, Y.M.; Tao, L.; Shan, H.H.; Wang, G.W.; Li, C.Y. Effect of pre-reduction on the performance of $\text{Fe}_2\text{O}_3/\text{Al}_2\text{O}_3$ catalysts in dehydrogenation of propane. *J. Mol. Catal. A Chem.* **2015**, *397*, 120–126. [[CrossRef](#)]
8. Cheng, M.; Zhao, H.H.; Yang, J.; Zhao, J.; Yan, L.; Song, H.L.; Chou, L.J. The catalytic dehydrogenation of isobutane and the stability enhancement over Fe incorporated SBA-15. *Microporous Mesoporous Mater.* **2018**, *266*, 117–125. [[CrossRef](#)]
9. Zhao, Z.J.; Wu, T.F.; Xiong, C.Y.; Sun, G.D.; Mu, R.T.; Zeng, L.; Gong, J.L. Hydroxyl-mediated non-oxidative propane dehydrogenation over $\text{VO}_x/\gamma\text{-Al}_2\text{O}_3$ catalysts with improved stability. *Angew. Chem. Int. Ed.* **2018**, *57*, 6791–6795. [[CrossRef](#)]
10. Cheng, E.; McCullough, L.; Noh, H.; Farha, O.; Hupp, J.; Notestein, J. Isobutane dehydrogenation over bulk and supported molybdenum sulfide catalysts. *Ind. Eng. Chem. Res.* **2020**, *59*, 1113–1122. [[CrossRef](#)]
11. Han, S.L.; Zhao, D.; Otroshchenko, T.; Lund, H.; Bentrup, U.; Kondratenko, V.A.; Rockstroh, N.; Bartling, S.; Doronkin, D.E.; Grunwaldt, J.; et al. Elucidating the nature of active sites and fundamentals for their creation in Zn-containing ZrO_2 -based catalysts for nonoxidative propane dehydrogenation. *ACS Catal.* **2020**, *10*, 8933–8949. [[CrossRef](#)]
12. Wang, Y.S.; Suo, Y.J.; Ren, J.T.; Wang, Z.; Yuan, Z.Y. Spatially isolated cobalt oxide sites derived from MOFs for direct propane dehydrogenation. *J. Colloid Interface. Sci.* **2021**, *594*, 113–121. [[CrossRef](#)] [[PubMed](#)]
13. Liu, G.; Zeng, L.; Zhao, Z.J.; Tian, H.; Wu, T.F.; Gong, J.L. Platinum-modified $\text{ZnO}/\text{Al}_2\text{O}_3$ for propane dehydrogenation: Minimized platinum usage and improved catalytic stability. *ACS Catal.* **2016**, *6*, 2158–2162. [[CrossRef](#)]
14. Cheng, M.; Zhao, H.H.; Yang, J.; Zhao, J.; Yan, L.; Song, H.L.; Chou, L.J. Facile synthesis of ordered mesoporous zinc alumina catalysts and their dehydrogenation behavior. *RSC Adv.* **2019**, *9*, 9828–9837. [[CrossRef](#)] [[PubMed](#)]
15. Li, J.; Chen, S.G.; Yang, N.; Deng, M.M.; Ibraheem, S.; Deng, J.H.; Li, J.; Li, L.; Wei, Z.D. Ultrahigh-loading zinc single-atom catalyst for highly efficient oxygen reduction in both acidic and alkaline media. *Angew. Chem. Int. Ed.* **2019**, *58*, 7035–7039. [[CrossRef](#)] [[PubMed](#)]
16. Shi, X.X.; Chen, S.; Li, S.; Yang, Y.Q.; Guan, Q.Q.; Ding, J.N.; Liu, X.Y.; Liu, Q.; Xu, W.L.; Lu, J.L. Particle size effect of SiO_2 -supported ZnO catalysts in propane dehydrogenation. *Catal. Sci. Technol.* **2023**, *13*, 1866–1873. [[CrossRef](#)]
17. Yang, F.W.; Zhang, J.; Shi, Z.B.; Chen, J.W.; Wang, G.; Zhao, J.Y.; Zhuo, R.S.; Wang, R.L. Regulation of active ZnO species on Si-based supports with diverse textural properties for efficient propane dehydrogenation. *ChemCatChem* **2023**, *15*, e2023004. [[CrossRef](#)]
18. Shan, F.K.; Shin, B.C.; Jang, S.W.; Yu, Y.S. Substrate effects of ZnO thin films prepared by PLD technique. *J. Eur. Ceram. Soc.* **2004**, *24*, 1015–1018. [[CrossRef](#)]
19. Sun, Y.N.; Gao, C.C.; Tao, L.; Wang, G.W.; Han, D.M.; Li, C.Y.; Shan, H.H. Zn-Nb-O catalysts for propylene production via catalytic dehydrogenation of propane. *Catal. Commun.* **2014**, *50*, 73–77. [[CrossRef](#)]
20. Yuan, Y.; Lobo, R.F. Zinc speciation and propane dehydrogenation in Zn/H-ZSM-5 catalysts. *ACS Catal.* **2023**, *13*, 4971–4984. [[CrossRef](#)]
21. Schweitzer, N.M.; Hu, B.; Das, U.; Kim, H.; Greeley, J.; Curtiss, L.A.; Stair, P.C.; Miller, J.T.; Hock, A.S. Propylene hydrogenation and propane dehydrogenation by a single-site Zn^{2+} on silica catalyst. *ACS Catal.* **2014**, *4*, 1091–1098. [[CrossRef](#)]
22. Almutairi, S.M.T.; Mezari, B.; Magusin, P.C.M.M.; Pidko, E.A.; Hensen, E.J.M. Structure and reactivity of Zn-modified ZSM-5 zeolites: The importance of clustered cationic Zn complexes. *ACS Catal.* **2012**, *2*, 71–83. [[CrossRef](#)]
23. Zhao, D.; Li, Y.; Han, S.; Zhang, Y.; Jiang, G.; Wang, Y.; Guo, K.; Zhao, Z.; Xu, C.; Li, R.; et al. ZnO Nanoparticles encapsulated in nitrogen-doped carbon material and silicalite-1 composites for efficient propane dehydrogenation. *iScience* **2019**, *13*, 269–276. [[CrossRef](#)] [[PubMed](#)]
24. Cao, T.L.; Dai, X.Y.; Fu, Y.; Qi, W. Coordination polymer-derived non-precious metal catalyst for propane dehydrogenation: Highly dispersed zinc anchored on N-doped carbon. *Appl. Surf. Sci.* **2023**, *607*, 155055. [[CrossRef](#)]
25. Feng, Q.P.; Xie, X.M.; Liu, Y.T.; Zhao, W.; Gao, Y.F. Synthesis of hyperbranched aromatic polyamide-imide and its grafting onto multiwalled carbon nanotubes. *J. Appl. Polym. Sci.* **2007**, *106*, 2413–2421. [[CrossRef](#)]

26. Duan, G.G.; Liu, S.W.; Jiang, S.H.; Hou, H.Q. High-performance polyamide-imide films and electrospun aligned nanofibers from an amide-containing diamine. *J. Mater. Sci.* **2019**, *54*, 6719–6727. [[CrossRef](#)]
27. Singh, K.; Nancy, Kaur, H.; Sharma, P.K.; Singh, G.; Singh, J. ZnO and cobalt decorated ZnO NPs: Synthesis, photocatalysis and antimicrobial applications. *Chemosphere* **2023**, *313*, 137322. [[CrossRef](#)]
28. Han, J.H.; Johnson, I.; Lu, Z.; Kudo, A.; Chen, M.W. Effect of local atomic structure on sodium ion storage in hard amorphous carbon. *Nano Lett.* **2021**, *21*, 6504–6510. [[CrossRef](#)]
29. Liu, Z.; Du, Z.Y.; Xing, W.; Yan, Z.F. Facial synthesis of N-doped microporous carbon derived from urea furfural resin with high CO₂ capture capacity. *Mater. Lett.* **2014**, *117*, 273–275. [[CrossRef](#)]
30. Cao, P.K.; Liu, Y.M.; Quan, X.; Zhao, J.J.; Chen, S.; Yu, H.T. Nitrogen-doped hierarchically porous carbon nanopolyhedras derived from core-shell ZIF-8@ZIF-8 single crystals for enhanced oxygen reduction reaction. *Catal. Today* **2019**, *327*, 366–373. [[CrossRef](#)]
31. Wang, L.H.; Han, X.D.; Zhang, Y.F.; Zheng, K.; Liu, P.; Zhang, Z. Asymmetrical quantum dot growth on tensile and compressive-strained ZnO nanowire surfaces. *Acta Mater.* **2011**, *59*, 651–657. [[CrossRef](#)]
32. Wong, T.I.; Tan, H.R.; Sentosa, D.; Wong, L.M.; Wang, S.J.; Feng, Y.P. Epitaxial growth of ZnO film on Si(111) with CeO₂(111) as buffer layer. *J. Phys. D Appl. Phys.* **2012**, *45*, 415306. [[CrossRef](#)]
33. Yu, J.G.; Xing, H.Z.; Zhao, Q.Q.; Mao, H.B.; Shen, Y.; Wang, J.Q.; Lai, Z.S.; Zhu, Z.Q. The origin of additional modes in Raman spectra of N⁺-implanted ZnO. *Solid State Commun.* **2006**, *138*, 502–504. [[CrossRef](#)]
34. Zhao, H.H.; Song, H.L.; Zhao, J.; Yang, J.; Yan, L.; Chou, L.J. The Reactivity and deactivation mechanism of Ru@C catalyst over hydrogenation of aromatics to cyclohexane derivatives. *ChemistrySelect* **2020**, *5*, 4316–4327. [[CrossRef](#)]
35. Liang, M.F.; Liu, Y.; Zhang, J.; Wang, F.Y.; Miao, Z.C.; Diao, L.C.; Mu, J.L.; Zhou, J.; Zhuo, S.P. Understanding the role of metal and N species in M@NC catalysts for electrochemical CO₂ reduction reaction. *Appl. Catal. B Environ.* **2022**, *306*, 121115. [[CrossRef](#)]
36. Gunawan, E.R.; Suhendra, D.; Hidayat, I.; Kurniawati, L. Optimization of alkyl diethanolamides synthesis from terminalia catappa L. kernel oil through enzymatic reaction. *J. Oleo Sci.* **2018**, *67*, 949–955. [[CrossRef](#)]
37. Przepiórski, J.; Skrodziewicz, M.; Morawski, A.W. High temperature ammonia treatment of activated carbon for enhancement of CO₂ adsorption. *Appl. Surf. Sci.* **2004**, *225*, 235–242. [[CrossRef](#)]
38. Qi, W.; Liu, W.; Zhang, B.S.; Gu, X.M.; Guo, X.L.; Su, D.S. Oxidative dehydrogenation on nanocarbon: Identification and quantification of active sites by chemical titration. *Angew. Chem. Int. Ed.* **2013**, *52*, 14224–14228. [[CrossRef](#)]
39. Sun, X.Y.; Li, B.; Su, D.S. Revealing the nature of the active site on the carbon catalyst for C-H bond activation. *Chem. Commun.* **2014**, *50*, 11016–11019. [[CrossRef](#)]
40. Zheng, F.C.; Yang, Y.; Chen, Q.W. High lithium anodic performance of highly nitrogen-doped porous carbon prepared from a metal-organic framework. *Nat. Commun.* **2014**, *5*, 5261. [[CrossRef](#)]
41. Guo, Q.Q.; Jing, W.; Hou, Y.Q.; Huang, Z.G.; Ma, G.; Han, X.J.; Sun, D.K. On the nature of oxygen groups for NH₃-SCR of NO over carbon at low temperatures. *Chem. Eng. J.* **2015**, *270*, 41–49. [[CrossRef](#)]
42. Ren, Y.J.; Zhang, F.; Hua, W.M.; Yue, Y.H.; Gao, Z. ZnO supported on high silica HZSM-5 as new catalysts for dehydrogenation of propane to propene in the presence of CO₂. *Catal. Today* **2009**, *148*, 316–322. [[CrossRef](#)]
43. Zhao, H.H.; Song, H.L.; Chou, L.J.; Zhao, J.; Yang, J.; Yan, L. Insight into the structure and molybdenum species in mesoporous molybdena-alumina catalysts for isobutane dehydrogenation. *Catal. Sci. Technol.* **2017**, *7*, 3258–3267. [[CrossRef](#)]
44. Zhang, J.; Liu, X.; Blume, R.; Zhang, A.H.; Schloegl, R.; Su, D.S. Surface-modified carbon nanotubes catalyze oxidative dehydrogenation of n-butane. *Science* **2008**, *322*, 73–77. [[CrossRef](#)] [[PubMed](#)]
45. Otroshchenko, T.; Jiang, G.; Kondratenko, V.A.; Rodemerck, U.; Kondratenko, E.V. Current status and perspectives in oxidative, non-oxidative and CO₂-mediated dehydrogenation of propane and isobutane over metal oxide catalysts. *Chem. Soc. Rev.* **2021**, *50*, 473–527. [[CrossRef](#)]

Disclaimer/Publisher's Note: The statements, opinions and data contained in all publications are solely those of the individual author(s) and contributor(s) and not of MDPI and/or the editor(s). MDPI and/or the editor(s) disclaim responsibility for any injury to people or property resulting from any ideas, methods, instructions or products referred to in the content.